Astronomy & Astrophysics manuscript no. sidorin_etal_2013_n107
February 25, 2014
©ESO 2014

Exploring GLIMPSE Bubble N107

Multiwavelength Observations and Simulations

V. Sidorin[1], K. A. Douglas[2,3,4], J. Palouš[1], R. Wünsch[1], and S. Ehlerová[1]

[1] Astronomical Institute of the Academy of Sciences of the Czech Republic, v. v. i., Boční II 1401/1a, 141 31, Praha 4, Czech Republic, e-mail: vojtech.sidorin@gmail.com
[2] Department of Physics and Astronomy, University of Calgary, 2500 University Dr NW, Calgary, Alberta, Canada, T2N 1N4
[3] Dominion Radio Astrophysical Observatory, PO Box 248, Penticton, B.C. Canada, V2A 6J9
[4] Okanagan College, 1000 KLO Road, Kelowna, B.C. Canada, V1Y 4X8

Accepted 11/02/2014

arXiv:1402.5614v1 [astro-ph.GA] 23 Feb 2014

ABSTRACT

Context. Bubble N107 was discovered in the infrared emission of dust in the Galactic Plane observed by the Spitzer Space Telescope (GLIMPSE survey: $l \approx 51\overset{\circ}{.}0$, $b \approx 0\overset{\circ}{.}1$). The bubble represents an example of shell-like structures found all over the Milky Way Galaxy.
Aims. We aim to analyse the atomic and molecular components of N107, as well as its radio continuum emission. With the help of numerical simulations, we aim to estimate the bubble age and other parameters which cannot be derived directly from observations.
Methods. From the observations of the H I (I-GALFA) and ^{13}CO (GRS) lines we derive the bubble's kinematical distance and masses of the atomic and molecular components. With the algorithm DENDROFIND, we decompose molecular material into individual clumps. From the continuum observations at 1420 MHz (VGPS) and 327 MHz (WSRT), we derive the radio flux density and the spectral index. With the numerical code *ring*, we simulate the evolution of stellar-blown bubbles similar to N107.
Results. The total H I mass associated with N107 is 5.4×10^3 $M_\odot$. The total mass of the molecular component (a mixture of cold gasses of H_2, CO, He and heavier elements) is 1.3×10^5 $M_\odot$, from which 4.0×10^4 $M_\odot$ is found along the bubble border. We identified 49 molecular clumps distributed along the bubble border, with the slope of the clump mass function of -1.1. The spectral index of -0.30 of a strong radio source located apparently within the bubble indicates nonthermal emission, hence part of the flux likely originates in a supernova remnant, not yet catalogued. The numerical simulations suggest N107 is likely less than 2.25 Myr old. Since first supernovae explode only after 3 Myr or later, no supernova remnant should be present within the bubble. It may be explained if there is a supernova remnant in the direction towards the bubble, however not associated with it.

Key words. ISM: bubbles – ISM: clouds – ISM: supernova remnants – H II regions

1. Introduction

Bubble N107 (SIMBAD: CPA2006 N107) is one of the largest bubbles in the catalogue by Churchwell et al. (2006). This catalogue is based on the infrared observations made with the Spitzer Space Telescope, (GLIMPSE survey, Benjamin et al. 2003) and contains more than 300 bubbles found in the interstellar medium (ISM) near the Galactic Plane. The catalogue was later expanded by Simpson et al. (2012) to more than 5000 bubbles, which were identified by a community of over 35 000 volunteers. These bubbles, with typical radii less than 10 pc, are examples of shell-like structures – features found in the ISM all over our Galaxy. Other examples are H I shells in catalogues by Heiles (1979, 1984); Ehlerová & Palouš (2005), with sizes up to 3500 pc; or dusty "loops" discovered in the IRAS full-sky survey by Kiss et al. (2004) and Könyves et al. (2007).

The varying sizes and masses of these structures suggest different mechanisms responsible for their creation. These mechanisms, which do not have to act solely, include:

1. feedback from massive (OB) stars: radiation, winds and supernovae (see refs. below);
2. infall of high-velocity clouds into the Galactic disc (e.g. Heiles 1984; Tenorio-Tagle & Bodenheimer 1988; Ehlerová & Palouš 1996);
3. energy and mass inserted by gamma-ray bursts (e.g. Efremov et al. 1998; Loeb & Perna 1998; Efremov et al. 1999); and
4. turbulence (Dib & Burkert 2005).

Bubble N107, as most of the GLIMPSE bubbles, is likely a result of stellar feedback (Churchwell et al. 2006; Deharveng et al. 2010), which may follow three different models:

1. An expanding H II region, assuming radiative heating and ionisation of hydrogen by UV photons from a massive star (Kahn 1954; Oort & Spitzer 1955; Spitzer 1978). The pressure inside the H II region is higher compared to the ambient neutral medium, so the H II region expands and collects the neutral material in an expanding shell.
2. A wind-blown bubble, supposing that energy is released via stellar winds (Castor et al. 1975; Weaver et al. 1977). Such a bubble, formed around a massive star, can be divided into several layers: an innermost layer, where the wind is freely expanding up to a layer of shocked stellar wind, where its kinetic energy is thermalised. This layer of the shocked wind is followed by a layer of swept up ISM, which in later stages of evolution is mainly atomic and molecular.
3. A supernova explosion, supposing an abrupt energy input into the ISM, producing an expanding shell/remnant (Chevalier 1974, and citations therein).

These different models of stellar feedback were also discussed by Tenorio-Tagle & Bodenheimer (1988); Ehlerová & Palouš (1996) and Efremov et al. (1999).

The shell-like structures can trigger star formation, since they consist of a layer of cold and dense material. In the so-called collect-and-collapse scenario (Elmegreen & Lada 1977; Elmegreen 1994; Whitworth et al. 1994), the shell fragments and creates a new generation of stars. Radiation driven implosion (Duvert et al. 1990; Lefloch & Lazareff 1994) considers the compression of preexisting condensations (globules) by the pressure of the ionised gas. A brief review of these and other triggering mechanisms is given in a study of GLIMPSE bubbles by Deharveng et al. (2010).

In this paper, we present a multiwavelength study of one of the largest GLIMPSE bubbles: N107, which lies in the central plane of the Galactic disc ($l \approx 51\overset{\circ}{.}0$, $b \approx 0\overset{\circ}{.}1$). A multiwavelength, colour picture of N107 is shown in fig. 1.

The paper is organised in the following way: In section 2, we complement the Spitzer infrared observations with H I line observations from the I-GALFA survey (Koo et al. 2010), ^{13}CO ($J = 1{-}0$) line observations from the GRS survey (Jackson et al. 2006) and radio continuum observations at 1420 and 327 MHz from the VGPS (Stil et al. 2006) and WSRT (Taylor et al. 1996) surveys. From the line observations, we derive the bubble's LSR[1] radial velocity (RV), kinematical distance and masses of the molecular and atomic components. From the radio continuum observations, we derive the flux densities and corresponding spectral indices of two radio sources lying apparently inside the bubble. In section 3, we use a recently published algorithm DENDROFIND (Wünsch et al. 2012) to decompose the molecular gas associated with the bubble into individual clumps and derive the slope of the clump mass function. In section 4, we use the numerical code *ring* (Palouš 1990; Ehlerová & Palouš 1996) to simulate the bubble's evolution in order to estimate its age, energy input and the size and mass of the molecular cloud from which the bubble evolved. Finally, a discussion and conclusions are presented in sections 5 and 6.

2. Observation of Bubble N107

2.1. Data Sources

GLIMPSE (Galactic Legacy Infrared Mid-Plane Survey Extraordinaire, Benjamin et al. 2003) and *MIPSGAL* (Carey et al. 2009) are two complementary infrared surveys mapping the Galactic disc with the Spitzer Space Telescope. GLIMPSE used instrument IRAC (Infrared Array Camera) which has four channels centred around 3.6, 4.5, 5.8 and 8.0 μm, for which the point response function FWHM is between 1.″7 and 2.″0. MIPSGAL used the instrument MIPS (Multiband Imaging Photometer for Spitzer) with a broadband channel centred around 24 μm, for which the point spread function FWHM is 6″.

I-GALFA (Inner-Galaxy ALFA Low-Latitude H I Survey, Koo et al. 2010) is part of a large project called GALFA-H I (Peek et al. 2011), which plans to map the entire sky observable by the Arecibo Observatory in the H I line. The FWHM beam size of the Arecibo telescope at 1420 MHz is 3.′35 with the GALFA-H I radial velocity channel width of 0.184 km/s. The data are provided in FITS cubes of the brightness temperature T_b. The single-channel standard deviation of the gaussian noise σ_noise is about 0.25 K.

[1] LSR = local standard of rest

The *GRS* (Galactic Ring Survey, Jackson et al. 2006) is a ^{13}CO ($J = 1{-}0$) survey focused on the Galactic molecular ring. The survey used the FCRAO 14-m telescope, with a FWHM beam size of 46″ and a radial velocity channel width of 0.21 km/s. The data are provided in FITS cubes of the antenna temperature T_A^*, with a typical noise $\sigma_\mathrm{noise}^* \approx 0.13$ K. We converted the data to the main-beam brightness temperature: $T_\mathrm{b} = T_\mathrm{A}^*/\eta_\mathrm{MB}$ and $\sigma_\mathrm{noise} = \sigma_\mathrm{noise}^*/\eta_\mathrm{MB}$, where $\eta_\mathrm{MB} = 0.48$ is the main beam efficiency (value suggested by Jackson et al. 2006).

VGPS (VLA Galactic Plane Survey, Stil et al. 2006) is a 1420 MHz continuum and H I line survey of the Galactic disc based on the interferometric observations done with the VLA (Karl G. Jansky Very Large Array). We use only the continuum observations since for the H I, data from I-GALFA are available with significantly lower noise. The FWHM beam size is 1′ and the gaussian noise is 0.3 K, for the continuum observations.

WSRT (Westerbork Synthesis Radio Telescope survey, Taylor et al. 1996) is a 327 MHz continuum survey of the Galactic plane utilising the WSRT interferometer in the Netherlands. The FWHM resolution is $1' \times (1'/\sin\delta)$ in the right ascension and declination (δ) direction, respectively. This yields for N107 ($\delta \approx 16°$) the FWHM resolution of $1' \times 3.'6$. The median gaussian noise is 2.5 mJy/beam.

The *UKIDSS* (UKIRT Infrared Deep Sky Survey) project is defined in Lawrence et al. (2007). UKIDSS uses the UKIRT (United Kingdom Infrared Telescope) Wide Field Camera (WFCAM; Casali et al. 2007) and a photometric system described in Hewett et al. (2006). The pipeline processing and science archive are described in Irwin et al. (2004) and Hambly et al. (2008). We used data from the 7th data release.

2.2. Dust Component

The bubble's outline is most prominent in the 8 μm maps from the GLIMPSE survey, where it was discovered by Churchwell et al. (2006), who derived its basic properties: mean position of $l \approx 51\overset{\circ}{.}0$, $b \approx 0\overset{\circ}{.}1$; mean radius of 11.′4 and a mean thickness of 2.′3. Most emission at 8 μm is coming from the bubble edges, forming a ring-like structure. The 8 μm channel is dominated by the emission of polycyclic aromatic hydrocarbons (PAHs) (Draine 2003; Reach et al. 2006, fig. 1; Pavlyuchenkov et al. 2013). PAHs, which are destroyed in the ionised regions, are tracing the photodissociation regions (PDRs), edges of molecular clouds illuminated by the UV radiation from a massive star. The UV radiation pervades the PDRs and excites the PAHs herein.

Counterpart emission at 24 μm was observed in MIPSGAL (Carey et al. 2009). Contrary to the 8 μm continuum, emission at 24 μm is filling part of the bubble's interior. The 24 μm continuum is dominated by the emission of very small grains – dust grains larger than PAHs – heated by a nearby massive star (Pavlyuchenkov et al. 2013).

A dark hole is present in the southwestern part of the bubble's interior. Almost no emission from dust, and also no emission of ^{13}CO or H I (see below), is observed there. Fig. 1 shows a multiwavelength, colour picture of N107 composed of the 8 μm and 24 μm continuum emission and the ^{13}CO line emission integrated over the radial velocities of 38.5 to 47.6 km/s.

2.3. Atomic Component

We searched the H I data cubes by eye for features possibly associated with bubble N107. An H I shell, morphologically similar

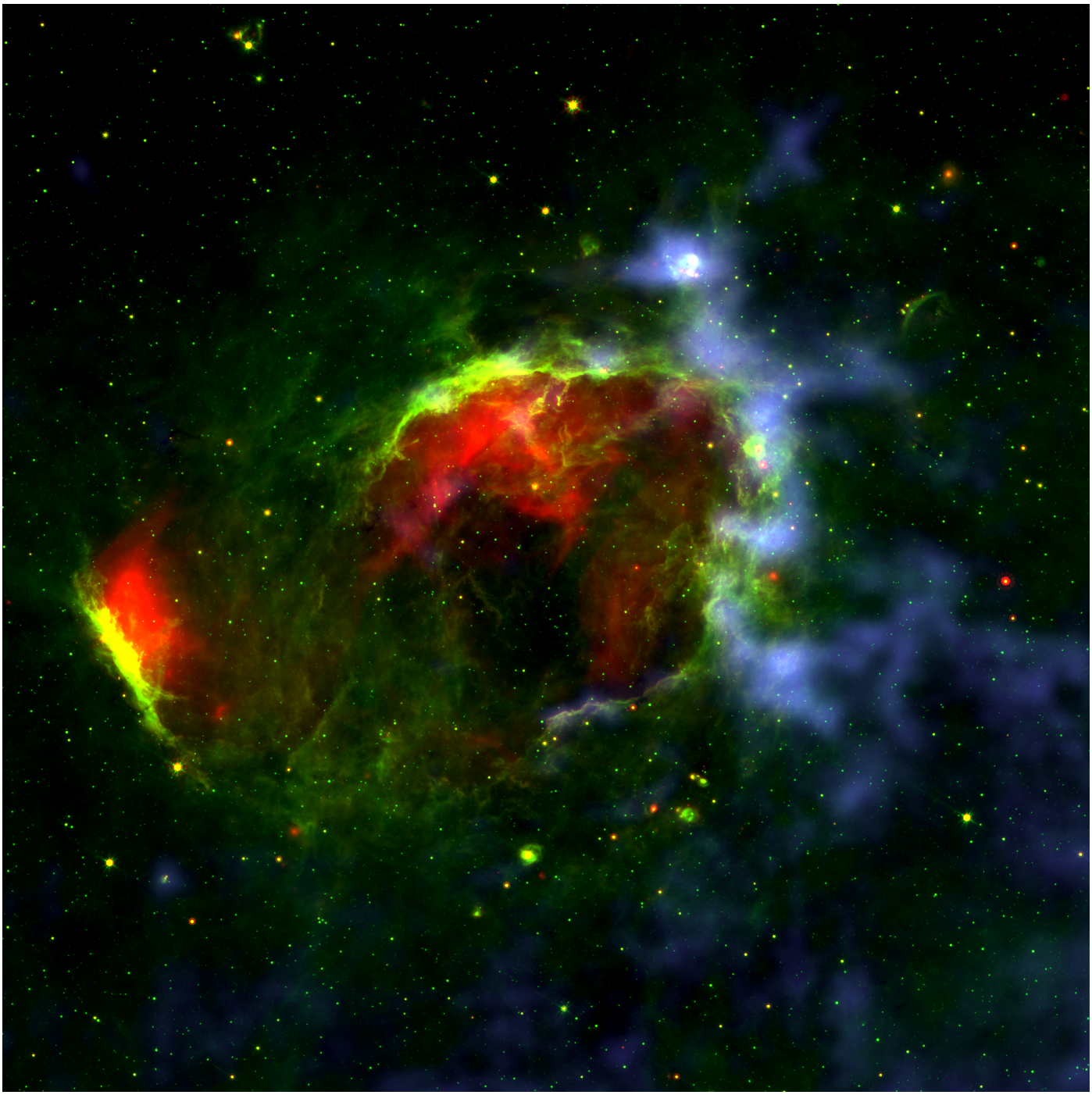

Fig. 1. Bubble N107 – false colour multiwavelength image. Red corresponds to 24 μm continuum, green to 8 μm continuum and blue to ^{13}CO (J = 1−0) line integrated over the radial velocities of 38.5 to 47.6 km/s. Note that the 24 μm continuum (red) is dominated by the emission of very small dust grains heated by a nearby massive star. The 8 μm continuum (green) is dominated by the emission of PAHs – large molecules found within molecular clouds. The emission of PAHs is tracing the photodissociation regions (PDRs) – edges of these clouds illuminated by UV radiation from a massive star. The CO line (blue) traces the cold gas of molecular clouds. The distinct red-green structure seen in the lower-left in the direction of the bubble's opening is likely not related to the bubble, since the radial velocity of the associated molecular material (≈ 60 km/s) differs significantly from the radial velocity of the N107 complex (≈ 43 km/s).

to N107, is located around the central LSR radial velocity of 43 km/s. Note that an incomplete ring of CO clumps is present at similar radial velocities (see sec. 2.4). The H I emission is located along the bubble edges, protruding outside farther than the CO emission, forming an atomic envelope of the whole structure. Maps of the H I brightness temperature in several velocity channels are shown in fig. 2.

Fig. 3 shows a map of the galactic longitude versus radial velocity (l–v diagram). The front wall is very faint, located at a radial velocity of ≈ 34 km/s. The back wall is more distinct, located at a radial velocity of ≈ 50 km/s. Between these radial velocities, a hole is apparent inside the bubble. The relative expansion velocity of the front versus back wall is ≈ 16 km/s.

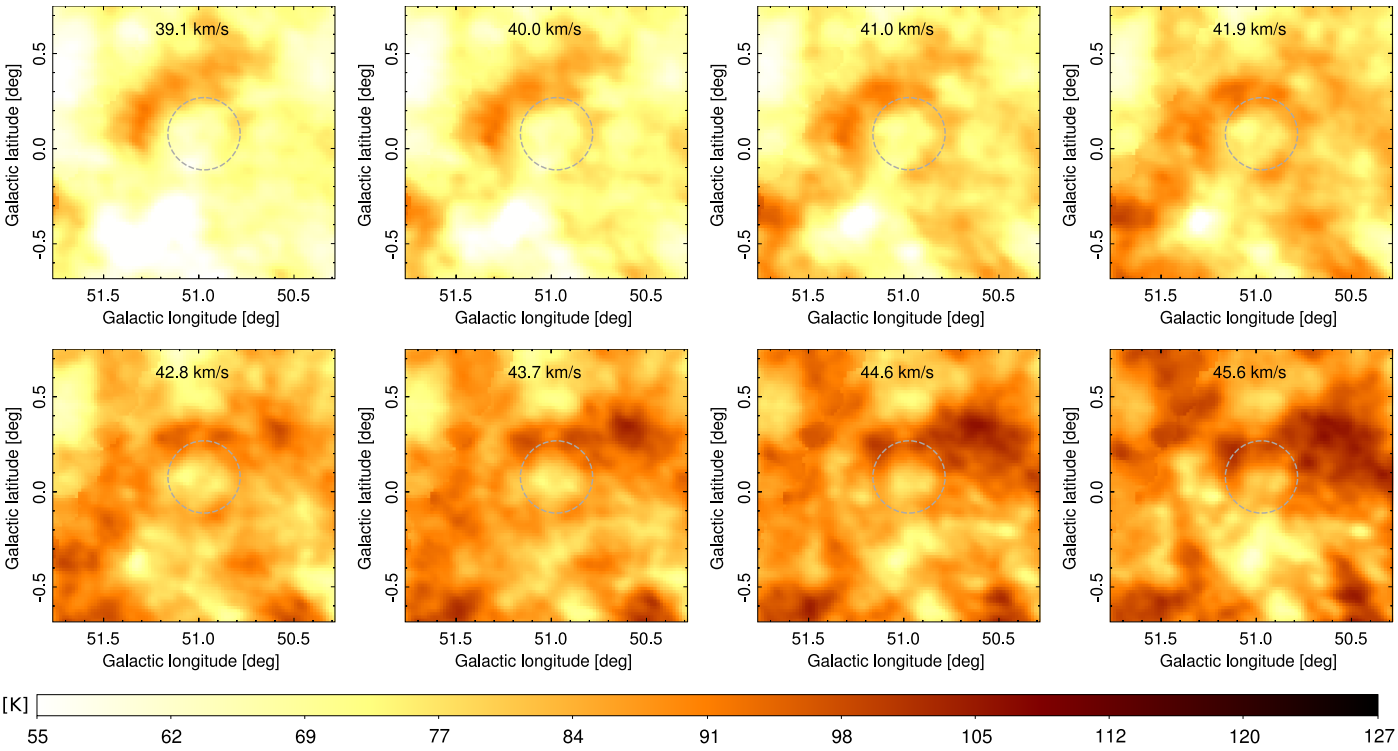

Fig. 2. Brightness temperature maps of the H I line in several velocity channels. An outline of bubble N107 as given in the catalogue of Churchwell et al. (2006) is marked with the dashed grey circle. Especially the channels 41.0 and 41.9 km/s show morphology similar to that of the 8 μm emission.

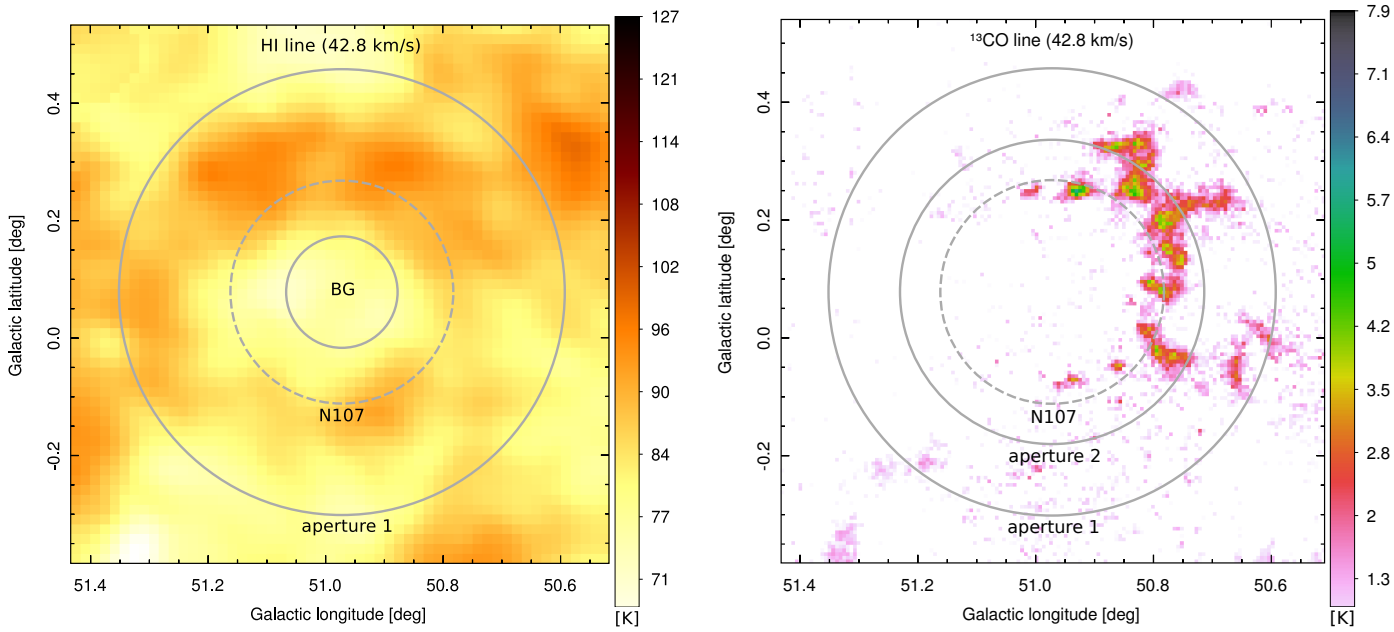

Fig. 4. Apertures for measuring the mass associated with bubble N107. The pixels lying within the apertures contribute to the measured masses. The dashed circles mark bubble N107 as was identified in the 8 μm emission by Churchwell et al. (2006). **Left:** H I line emission at 42.8 km/s. The innermost circle (BG) is the region we used to derive the background emission. **Right:** ^{13}CO line emission at 42.8 km/s. We use two apertures for measuring the molecular mass. Aperture 1 is same as that for measuring the H I mass, while aperture 2 is smaller and covers only the immediate vicinity of the bubble.

In order to measure the H I mass associated with the bubble, we define the following 3D aperture (aperture 1, see also fig. 4, left panel): radius of two times that of N107, $r_{\rm ap1} = 2 \cdot r_{\rm N107} = 22\farcm8$, and the radial velocity channels from 32.7 to 52.0 km/s inclusive. All the pixels lying within this aperture contribute to the measured H I mass.

To derive the mass of the neutral hydrogen, we use the optically thin limit of H I line radiative transfer. Then, the H I column

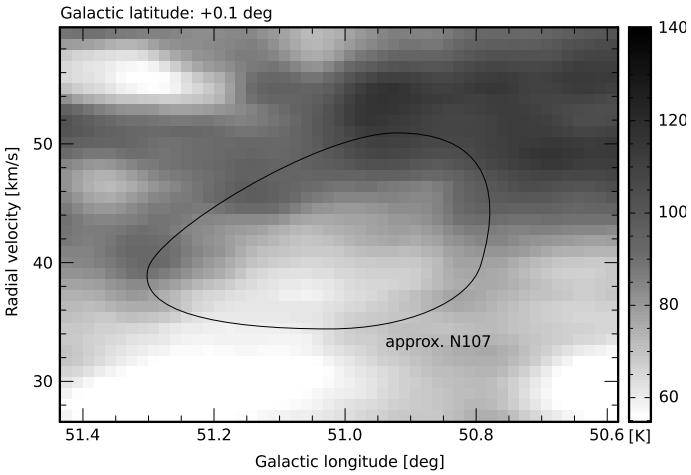

Fig. 3. Brightness temperature of the H I line in an *l*–*v* diagram: a cut through $b = 0.^{\circ}1$. The black curve marks the approximate extent of the H I shell associated with N107.

density $N_{\mathrm{H\,I}}$ can be computed from the formula (Rohlfs & Wilson 1996):

$$\frac{N_{\mathrm{H\,I}}}{\mathrm{cm}^{-2}} = 1.8 \times 10^{18} \int \frac{T_\mathrm{b}}{\mathrm{K}} \frac{\mathrm{d}v}{\mathrm{km/s}}, \tag{1}$$

where T_b is the observed brightness temperature of the H I gas and, in our case of an I-GALFA data cube, the integral takes form of a sum over a set of pixels with $\mathrm{d}v = 0.184$ km/s.

The Galactic H I emission has a strong background component. To estimate it, we assume that the bubble's interior is evacuated, so the H I emission observed apparently near the bubble centre is due to this H I background, not associated with the bubble. We defined another 3D aperture with the radius half that of the N107 and the radial velocity channels from 39.1 to 43.7 km/s (see fig. 4). This aperture encloses a volume in the central part of the bubble. The mean T_b within this region is 72 K, which we adopt as the H I background component and subtract it before computing the mass.

Furthermore, in the process of mass derivation, we need to know the **distance to N107**. Considering also the ^{13}CO emission (see below), we adopt the central radial velocity of 42.8 km/s. The Galactic rotation model of Brand & Blitz (1993) gives for that radial velocity two kinematical distances: 3.6 and 7.1 kpc. We adopt the near one of 3.6 kpc, which yields the bubble mean radius of 11.9 pc (11.4′). The near distance is favoured by the estimated virial masses of the molecular clumps found along the bubble borders. For the far distance of 7.1 kpc, we got 22 of 49 clumps with supervirial masses, while for the near distance of 3.6 kpc, we got only 2 clumps with virial masses above 1 (clumps 7 and 21 in tab. A.1). Note that Churchwell et al. (2006) suggest distances of 4.7/6.0 kpc. They use the same rotation model as we do, however with a less reliable determination of the radial velocity obtained from the observation of coincident H II regions. They advocate also the near kinematical distance.

To estimate the uncertainty of the measured mass, we use the standard Taylor formula:

$$\sigma_f = \sqrt{\sum_i \left(\frac{\partial f}{\partial x_i}\right)^2 \sigma_{x_i}^2}, \tag{2}$$

where f is the measured value (in our case the H I mass), σ_f is its uncertainty, which is derived from uncertainties σ_{x_i} of variables x_i on which f depends (in our case e.g. the distance to N107).

The resulting H I mass associated with N107, i.e. the total H I mass within aperture 1 after subtracting the background, is $5.4 \times 10^3\ M_\odot$. The major sources of uncertainty are the distance to N107 and the background emission. Assuming the distance uncertainty of 10 % (0.36 kpc) and the background uncertainty of 1 K, the total H I mass uncertainty is about 20 %, i.e. $1 \times 10^3\ M_\odot$.

2.4. Molecular Component

Around the radial velocity of 43 km/s, CO emission is present along the bubble borders. Maps of the CO emission (fig. 5) show that CO gas forms clumps, which are distributed in a ring-like structure along the edges of the bubble, protruding outside. Almost no emission is coming from the interior. Around the radial velocity of 48 km/s, the CO emission merges with another complex of molecular clouds, while in the channels below 38 km/s, CO emission vanishes.

To measure the associated molecular mass, we use two 3D apertures (see fig. 4, right panel). Aperture 1 is same as that for measuring the H I mass. Aperture 2 is smaller, with radius $r_{\mathrm{ap2}} = 1.36 \cdot r_{\mathrm{N107}} = 15.'5$, radial velocity channels from 38.8 to 46.9 km/s inclusive and covers only the immediate vicinity of the bubble, i.e. only the mass accumulated in the expanding shell. Note that for comparing the observation and simulations, we use the molecular mass found within aperture 2. We treat the radiative transfer in the line of ^{13}CO ($J = 1{-}0$), described in Rohlfs & Wilson (1996). First, we derive the optical depth:

$$\tau = -\ln\left[1 - \frac{T_\mathrm{b}}{T_0}\left\{\left[\mathrm{e}^{T_0/T_\mathrm{ex}} - 1\right]^{-1} - \left[\mathrm{e}^{T_0/T_\mathrm{CMB}} - 1\right]^{-1}\right\}^{-1}\right], \tag{3}$$

where T_ex is the excitation temperature, which we assume to be 20 K. T_b is the brightness temperature of the CO line; $T_\mathrm{CMB} = 2.7$ K is the temperature of the cosmic microwave background and

$$T_0 = \frac{hf}{k} \approx 5.3\ \mathrm{K}, \tag{4}$$

where h is the Planck constant; k is the Boltzmann constant and $f = 110$ GHz is the ^{13}CO ($J = 1{-}0$) line frequency. Assuming local thermodynamical equilibrium, characterised by a single excitation temperature T_ex, we can compute the ^{13}CO column density from the formula (Rohlfs & Wilson 1996):

$$\frac{N_{^{13}\mathrm{CO}}}{\mathrm{cm}^{-2}} = 2.6 \times 10^{14} \frac{T_\mathrm{ex}}{1 - \mathrm{e}^{-T_0/T_\mathrm{ex}}} \int \tau(v)\, \mathrm{d}v, \tag{5}$$

where, in our case of the GRS data cube, $\mathrm{d}v = 0.21$ km/s and the integral becomes a sum over a desired range of pixels. From the ^{13}CO column density, the H_2 column density is derived assuming the abundance (Binney & Merrifield 1998) $N_{\mathrm{H_2}} = 6.5 \times 10^5 N_{^{13}\mathrm{CO}}$. Finally, the total mass of the molecular matter m_mol is computed using the standard solar hydrogen abundance X:

$$m_\mathrm{mol} = \frac{m_{\mathrm{H_2}}}{X}, \qquad \text{where} \quad X = 0.735, \tag{6}$$

and $m_{\mathrm{H_2}}$ is the mass in the form of the molecular hydrogen. Note that we use term *molecular matter* or *molecular mass* to refer to the matter found in molecular clouds, i.e. a mixture of H_2, He,

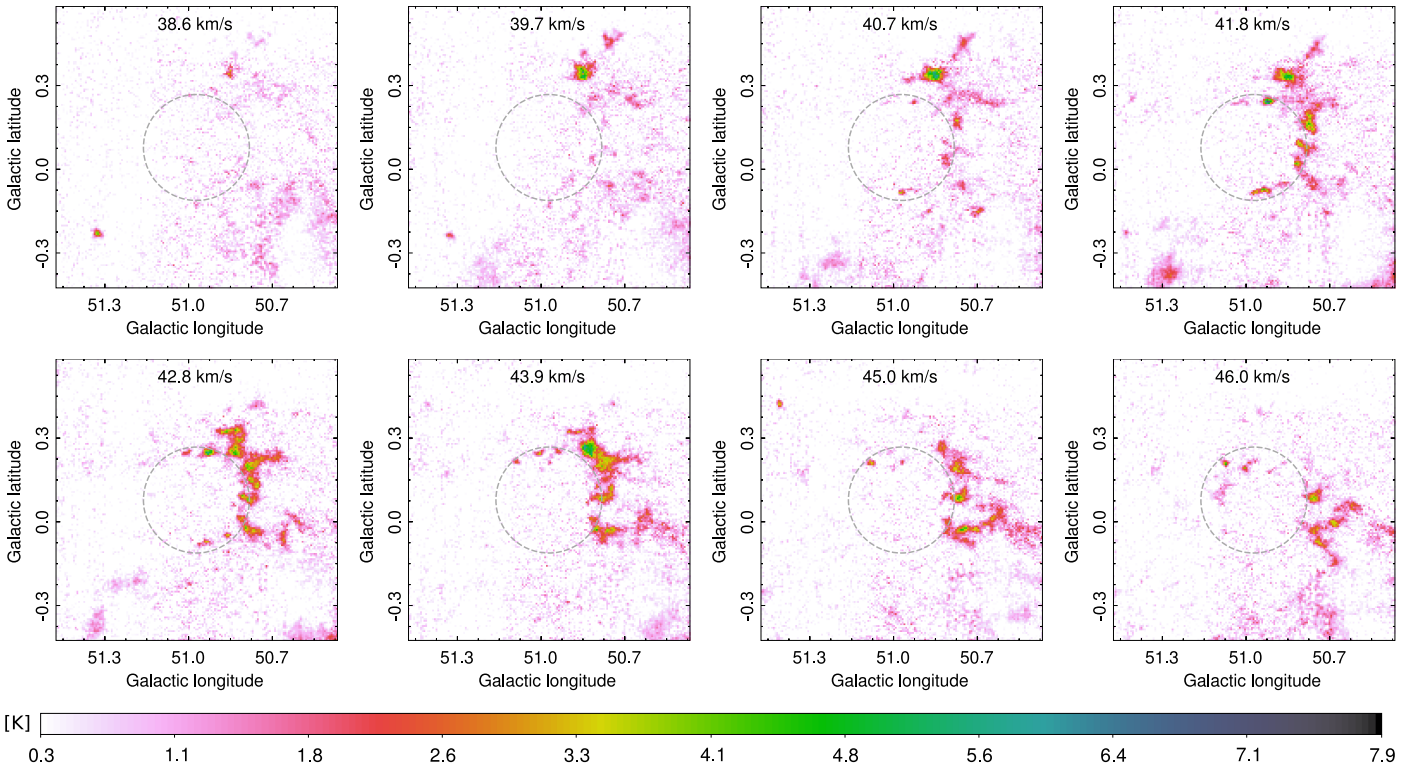

Fig. 5. Brightness temperature maps of the ^{13}CO (J = 1–0) emission in several velocity channels. The units is kelvin. An outline of bubble N107 as given in the catalogue of Churchwell et al. (2006) is marked with the dashed grey circle.

CO and trace amounts of other molecules, elements and dust. The distance to N107 (3.6 kpc) is discussed above in section 2.3.

The total molecular mass within aperture 1 is 1.3×10^5 $M_\odot$, from which 9.8×10^4 $M_\odot$ in in the form of H_2, rest in helium and heavier elements. The total molecular mass within aperture 2 (in the expanding shell only) is 4.0×10^4 $M_\odot$, from which $2.9{\times}10^4$ $M_\odot$ is in the form of H_2. The major source of uncertainty is the ^{13}CO abundance. We used $N_{H_2} = 6.5{\times}10^5 N_{^{13}CO}$ (Binney & Merrifield 1998). Observations and models show, however, that the abundance varies for different clouds and depends also on the physical conditions inside individual clumps (Sonnentrucker et al. 2007; Visser et al. 2009; Wilson 1999). Another source of the uncertainty we consider is the distance to N107. Using eq. 2 and assuming the ^{13}CO abundance uncertainty of 20 % and the distance uncertainty of 10 % (0.36 kpc), the uncertainty of the molecular masses given above is about 30 %.

2.5. Radio Continuum and Spectral Index

Since an H II region was identified in the direction of the bubble (Paladini et al. 2003, region 576) and also the 24 μm emission is present inside the bubble, we expected to observe its radio continuum counterpart.

Both the VGPS (1420 MHz) and WSRT (327 MHz) surveys show a distinct diffuse radio source located apparently within the bubble, in its eastern (left) part, slightly below the area, where the 24 μm emission is strongest (see fig. 6). Beside this source, the bubble interior is filled with much fainter radio emission. Another diffuse radio source is present further east of the bubble ($l \approx 51.^\circ35$, $b \approx 0^\circ$). This source is associated with a complex of molecular material found at radial velocities of about 60 km/s, so it is likely not associated with the bubble. Fig. 7 shows a comparison of the VGPS radio continuum with the emission at 8 μm and 24 μm. Inside the bubble, the radio continuum follows the bubble outline defined by the PAHs emission at 8 μm. In the northern (top) and western (right) part, the radio continuum is mixed with the emission of very small grains at 24 μm, while in the eastern part (left), the 24 μm emission vanishes and only the radio continuum is observed.

We measured the radio flux densities in four regions: two located apparently within the bubble – defined by apertures A and B – and two located outside the bubble – defined by apertures C and D (fig. 6). Aperture A covers the distinct source in the eastern part of the bubble (source "A"), while aperture B covers the faint emission in its western (right) part (source "B"). Aperture C covers part of the fainter emission outside the bubble (source "C") and aperture D covers the distinct radio source located eastern of the bubble (source "D"). We subtracted a background derived from flux within an aperture covering a relatively homogeneous region free of visible radio sources (fig. 6). Then we used the two fluxes at 1420 and 327 MHz to derive the spectral index α for both sources A and B:

$$\alpha = \frac{\ln S_1 - \ln S_2}{\ln f_1 - \ln f_2}, \tag{7}$$

where S_1, S_2 are the fluxes at frequencies f_1, f_2. Note that the theoretical spectral index for a classical H II region in the optically thin limit is −0.1 (Condon & Ransom 2010), although the usually observed values are around 0 or more (Rohlfs & Wilson 1996; Kellermann & Verschuur 1988). In distinction to H II regions, the mean observed spectral index of supernova remnants is −0.5 (average value in catalogue of Green 2009). The measured flux densities and the derived spectral indices are presented in table 1.

The spectral index of source A of −0.3 suggests a nonthermal (synchrotron) contribution to the received radio flux: a supernova

Table 1. Radio continuum flux densities and spectral indices for apertures A, B, C and D. The flux densities ($S_{\mathrm{A,B,C,D}}$) are background-subtracted.

Frequency	S_{A}	S_{B}	S_{C}	S_{D}
1420 MHz	11.30 Jy	2.81 Jy	2.87 Jy	5.12 Jy
327 MHz	17.55 Jy	2.74 Jy	3.91 Jy	6.19 Jy
Spectral index	−0.30	0.02	−0.21	−0.13

remnant. No known supernova remnant is associated, yet, with that radio source. For source B, the spectral index of ≈ 0 suggests a thermal origin of the flux: a classical H II region. The spectral indices of sources C (−0.2) and D (−0.1) suggest that part of their emission is also nonthermal.

3. Analysis of Molecular Clumps

We decomposed the molecular ring associated with N107 into individual molecular clumps with the program DENDROFIND, described in the appendix of Wünsch et al. (2012). DENDROFIND processes data cubes – typically position-position-velocity data cubes of the brightness temperature T_{b} – and outputs a list of molecular clumps organised in a hierarchical structure, which can be represented by a dendrogram (Rosolowsky et al. 2008). In our case, the data cube is a cutout of the ^{13}CO GRS data and has two spatial dimensions (galactic longitude, galactic latitude) and one radial velocity dimension. Each clump consists of a dense core surrounded by a less dense molecular envelope. The core is observed as a local T_{b} peak. DENDROFIND is controlled by four parameters: `Nlevels` sets the number of steps by which it goes through the data cube when searching for clump peaks; `Npxmin` sets the minimal number of pixels which can form a clump; `Tcutoff` sets the minimal T_{b} which is yet considered a signal, pixels with lower T_{b} are discarded; `dTleaf` sets the minimal height of a local peak to be considered a clump's core; a higher `dTleaf` will merge more clumps. Parameters `Tcutoff` and `dTleaf` are designed to be set to a value of ≈ 3 × the noise level. We ran DENDROFIND with the following parameters: `Nlevels` = 1000, `Npixmin` = 5, `Tcutoff` = `dTleaf` = 1.0 ≈ $3\sigma_{\mathrm{noise}}$, where $\sigma_{\mathrm{noise}} \approx 0.34$ K is the estimated standard deviation of the gaussian noise found within our N107 cutout of the ^{13}CO GRS data. Note that this value is slightly greater then the 'typical' value of the entire GRS of 0.27 K given in the paper of Jackson et al. (2006).

In order to select only the clumps associated with bubble N107, we took only those clumps of which cores lie within the aperture 2 used for measuring the total molecular mass (sec. 2.4).

Table 2 lists the identified molecular clumps. Note that only the first 10 clumps with the highest core T_{b} are shown there; a complete list is available in an online appendix (tab. A.1). The meaning of the columns is as follows: N is the number identifying a clump in our list; l_{peak}, b_{peak}, v_{peak} are the galactic longitude, galactic latitude and LSR radial velocity, respectively, of the brightest pixel of the clump. T_{peak} is the brightness temperature of the brightest pixel. R is the clump equivalent radius, defined as

$$R = \sqrt{A_{\mathrm{cl}}/\pi}, \tag{8}$$

where A_{cl} is the clump projected area in the sky. $FWHM$ is the clump full width at half maximum computed as

$$FWHM_x = 2\sqrt{2\ln 2}\sqrt{\sigma_x^2 + \left(\frac{\Delta x}{2\sqrt{2\ln 2}}\right)^2}, \tag{9}$$

where $x \in \{l,\ b,\ v\}$. The second term under the big square root represents the pixel resolution term and ensures that the $FWHM$ is not smaller than the pixel size. For the GRS data cube, the pixel size Δx is $22\farcs1 \times 22\farcs1 \times 0.21$ km/s, which corresponds at N107's distance of 3600 pc to 0.39 pc × 0.39 pc × 0.21 km/s. If Δx goes to zero, the $FWHM$ approaches the gaussian $FWHM$. σ_x^2 is the variance weighted by the brightness temperature T_{b}:

$$\sigma_x^2 = \overline{x^2} - \overline{x}^2 = \sum_{\mathrm{pix}} \frac{x^2 T_{\mathrm{b}}}{T_{\mathrm{tot}}} - \left(\sum_{\mathrm{pix}} \frac{x T_{\mathrm{b}}}{T_{\mathrm{tot}}}\right)^2. \tag{10}$$

$$\text{where} \quad T_{\mathrm{tot}} = \sum_{\mathrm{pix}} T_{\mathrm{b}}, \tag{11}$$

with the summation taken over all pixels belonging to the clump. M is the clump mass, which is the total mass of pixels belonging to the clump, derived from equations 3–6 (sec. 2.4). The error of the clump mass, assuming gaussian noise and neglecting pixel correlation within the beam, is

$$\Delta M = \sqrt{N_{\mathrm{px}}}\,\Delta M_{\mathrm{px}}, \tag{12}$$

where N_{px} is the number of pixels of the clump and ΔM_{px} is the σ_{noise} equivalent mass. In our case of the GRS ^{13}CO data cubes, $\sigma_{\mathrm{noise}} = 0.34$ K $\Rightarrow \Delta M_{\mathrm{px}} = 0.21\ M_\odot$. M_{vir} is the clump virial mass, estimated as (MacLaren et al. 1988):

$$M_{\mathrm{vir}} = 190 \cdot R \cdot FWHM_v^2. \tag{13}$$

The formula above assumes a spherical clump with a density profile $\propto 1/r$. ΔM_{vir} is the virial mass error derived from the first order Taylor expansion of eq. 13, assuming the clump's area and $FWHM_v$ errors of one pixel.

Fig. 8 shows a histogram of clumps masses. Overlaid is a line representing a fit by a function $\mathrm{d}N/\mathrm{d}M = C(M/M_\odot)^\alpha$, where α is the slope of the clump mass function and C is some constant. We used least-square fitting on a logarithmic scale, i.e. we fit the log of the bin heights $\log(\mathrm{d}N/\mathrm{d}M)$ by a function $\log(C(M/M_\odot)^\alpha)$. The best fitting slope is $\alpha = -1.1$. The bins in the histogram have variable widths, set so that each contains 7 clumps. This ensures that all bins have the same significance.

4. Numerical Simulations of Bubbles and Comparison with N107

We simulated the evolution of bubbles formed in the ISM around massive stars in order to estimate parameters of N107, which cannot be derived directly from observation (esp. its age). We used a version of the FORTRAN code *ring* (Palouš 1990; Ehlerová & Palouš 1996), which was originally written for simulations of expanding H I shells in the Galactic ISM.

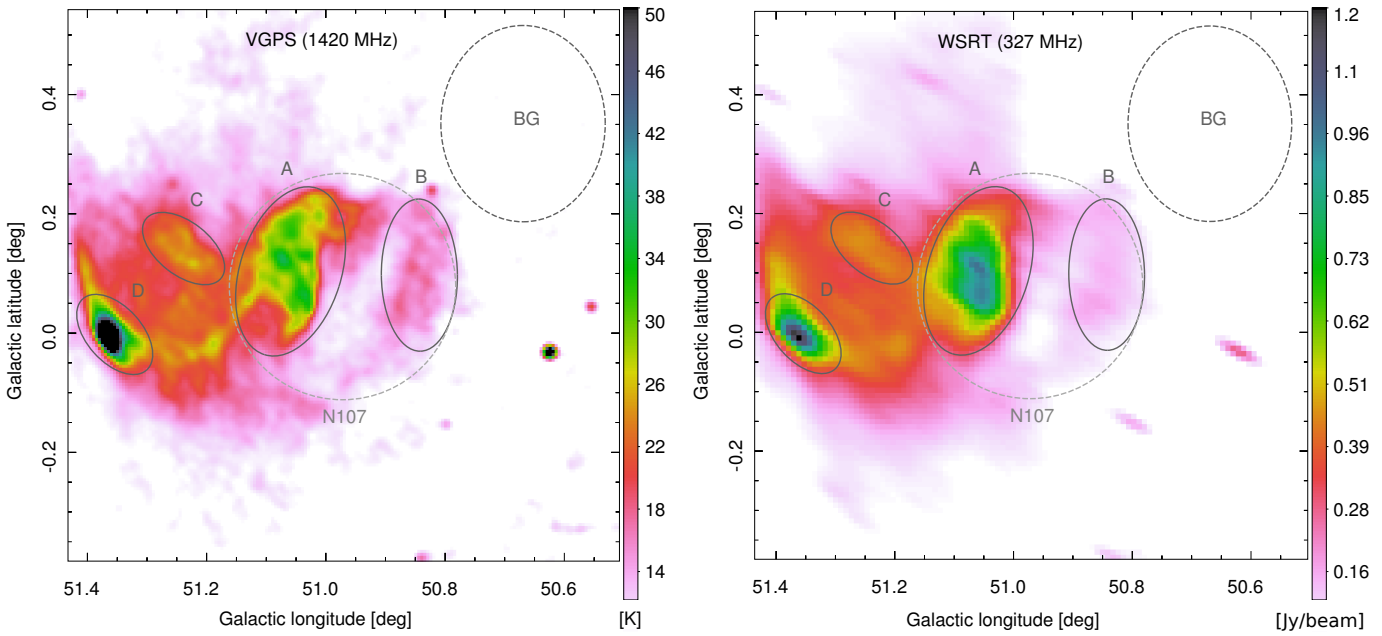

Fig. 6. Radio continuum emission associated with bubble N107. The bubble is denoted by the grey dashed circle in the centre. Overlaid are four elliptical apertures (A, B, C, D) used to measure the radio fluxes. The grey dashed ellipse in the upper right (labelled BG) is the region used for measuring the background. **Left:** Emission at 1420 MHz/21 cm from the VGPS survey. **Right:** Emission at 327 MHz/92 cm from the WSRT survey. Note blurring in the direction of declination (top-left–to–bottom-right), caused by the larger beam size (lower resolution) in the declination direction.

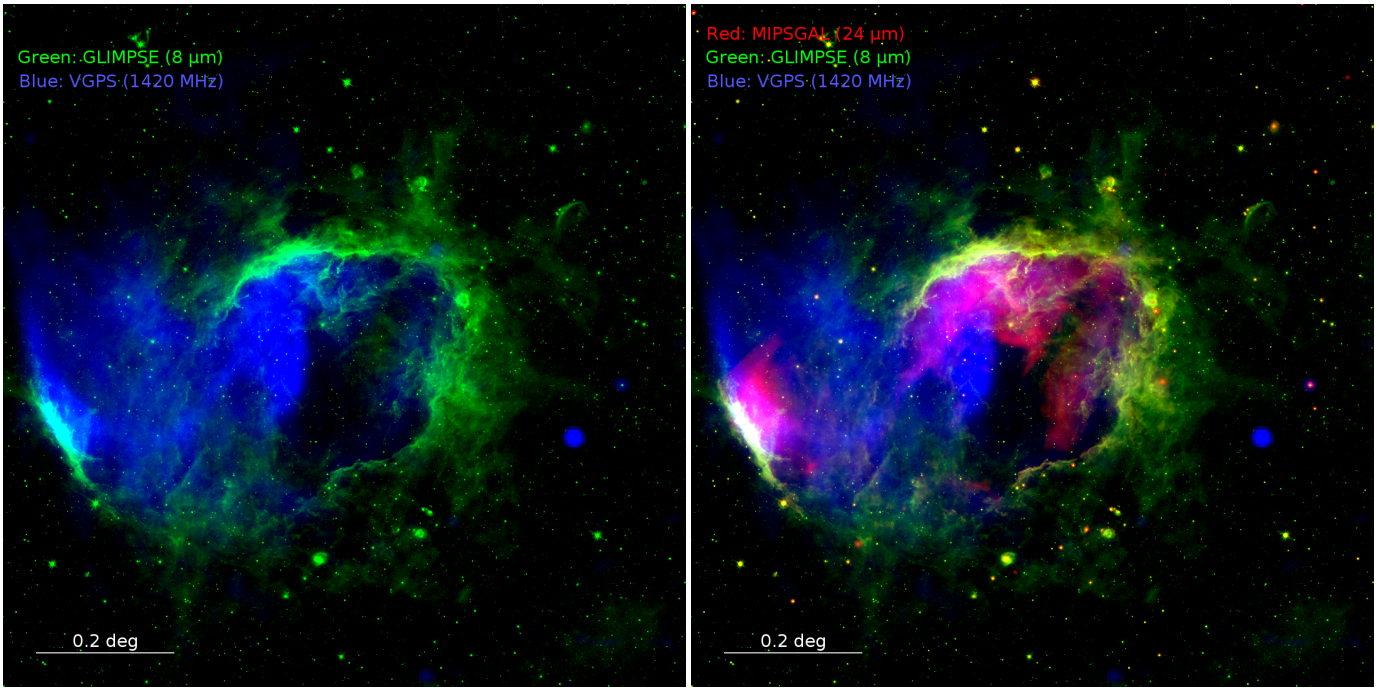

Fig. 7. Comparison of the VGPS radio continuum at 1420 MHz/21 cm (blue) with the 8 μm (green) and 24 μm (red) emission. **Left:** 1420 MHz and 8 μm emission. The radio continuum follows the bubble outline and fills part of its interior. **Right:** Same as left with added 24 μm emission. Inside the bubble, the radio continuum is well correlated with the 24 μm emission, except for the eastern part, where the 24 μm emission is absent and only the radio continuum is observed.

4.1. Code Description

The simulation starts with a small spherical shell, which is set according to the wind-blown bubble model of Weaver et al. (1977) in the pressure-driven snowplough phase. The infinitesimally thin shell (thin-shell approximation) is divided into $nl \times np$ elements. We solve the equations of motion including the pressure difference between the shell interior and exterior and the mass accumulation of the ambient medium. We do not include gravity or any other force acting on the shell. The momentum equation for an element is

$$\frac{\mathrm{d}}{\mathrm{d}t}(m\mathbf{v}) = \mathbf{S}(P_\mathrm{i} - P_\mathrm{e}), \tag{14}$$

Table 2. Molecular clumps associated with bubble N107. The first column gives a number identifying a clump in our list. The meaning of other columns is explained in sec. 3. Only the first 10 clumps are show here; a full table is available in online appendix (tab. A.1).

N	$\frac{l_{\rm peak}}{\rm deg}$	$\frac{b_{\rm peak}}{\rm deg}$	$\frac{v_{\rm peak}}{\rm km\ s^{-1}}$	$\frac{T_{\rm peak}}{\rm K}$	$\frac{R}{\rm pc}$	$\frac{\rm FWHM_l}{\rm pc}$	$\frac{\rm FWHM_b}{\rm pc}$	$\frac{\rm FWHM_v}{\rm km\ s^{-1}}$	$\frac{M}{M_\odot}$	$\frac{\Delta M}{M_\odot}$	$\frac{M_{\rm vir}}{M_\odot}$	$\frac{\Delta M_{\rm vir}}{M_\odot}$	$\frac{M}{M_{\rm vir}}$
1	50.919	0.241	41.89	7.0	2.2	2.45	1.62	1.84	1037.1	5.6	1409.9	324.8	0.736
2	50.840	0.266	44.01	5.8	4.0	3.48	3.40	2.83	4082.1	11.5	6050.2	909.0	0.675
3	50.753	-0.029	45.08	4.7	3.2	3.38	2.52	4.63	3119.8	10.8	12847.9	1180.5	0.243
4	51.073	0.204	45.93	4.7	1.2	1.41	0.99	2.57	351.1	3.6	1494.4	247.5	0.235
5	50.766	0.081	45.50	4.6	3.3	3.66	2.21	3.92	3469.1	10.9	9622.4	1044.0	0.361
6	50.938	-0.072	42.31	4.6	1.8	3.06	1.17	1.70	635.2	4.8	1010.1	252.4	0.629
7	50.778	0.192	42.74	4.5	5.0	5.15	5.07	2.76	7365.5	15.9	7259.4	1120.0	1.015
8	50.815	0.020	42.10	4.5	2.3	1.59	2.60	3.91	1206.7	6.8	6597.7	716.4	0.183
9	50.803	-0.029	44.01	4.4	2.3	2.05	2.11	2.26	1059.1	6.1	2272.7	428.0	0.466
10	50.999	0.247	43.59	3.6	1.4	2.08	1.08	2.26	276.5	3.5	1343.3	252.2	0.206
...							...						...

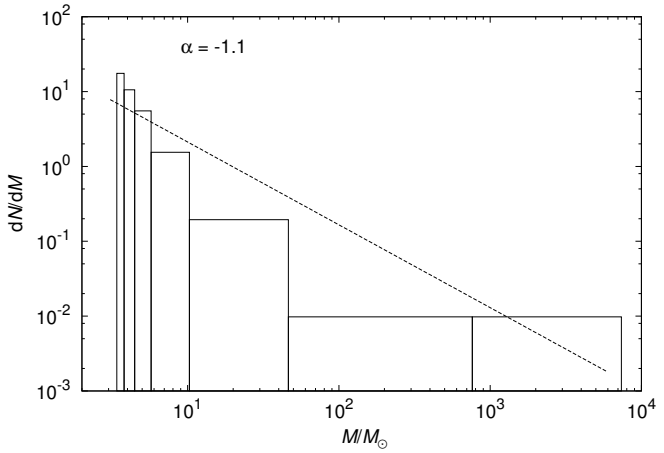

Fig. 8. Histogram of the mass spectrum of molecular clumps associated with bubble N107. The bin widths are variable, set so that each bin contains 7 clumps. The dashed line represents the best fitting power-law function with the index $\alpha = -1.1$.

where m is the element mass, $\mathbf{v}$ is the element velocity, $\mathbf{S}$ is the element surface and $P_{\rm i}$ and $P_{\rm e}$ are the interior and exterior pressures. The total number of elements is fixed (we used 30×60), so their surface and mass grow with time. The mass growth is given by the equation

$$\frac{{\rm d}m}{{\rm d}t} = \rho(\mathbf{v} \cdot \mathbf{S}), \tag{15}$$

where ρ is the local density of the ambient medium.

For the sake of simplicity, an energy source is represented as a continuous and constant energy input $\dot{E}$. For each timestep a corresponding amount of energy is added to the bubble interior and a new value of the interior pressure is computed as

$$P_{\rm i} = \frac{2}{3}\frac{E_{\rm i}}{V}, \tag{16}$$

where $E_{\rm i}$ is the interior thermal energy and V is the bubble volume. Eq. 16 assumes that the interior is filled with monoatomic gas expanding adiabatically. In the case of a shell expanding into a uniform medium, this type of energy source gives for the shell radius, as a function of time, a power-law with an index 3/5. This is in between the power-law index 2/5, given by a single (supernova) explosion and the power-law index 4/7, valid for an expanding H II region.

The motion of the bubble elements is integrated using the fourth-order Runge-Kutta method with adaptive timestep.

4.2. Simulation Setup

We assume a bubble expanding in a molecular cloud with a 3D gaussian density profile (see fig. 9):

$$n = n_0 \exp\left\{-\frac{1}{2}\left[\left(\frac{x-x_0}{\sigma_x}\right)^2 + \left(\frac{y-y_0}{\sigma_y}\right)^2 + \left(\frac{z-z_0}{\sigma_z}\right)^2\right]\right\}, \tag{17}$$

where n is the particle density, n_0 is the particle density in the centre of the cloud; $\sigma_x, \sigma_y, \sigma_z$ are the gaussian thicknesses (standard deviation) in the x, y, z direction; x_0, y_0, z_0 specify the location of the cloud centre.

We also assume the centre of expansion is shifted/dislocated from the centre of the cloud by Δr_0 towards direction $(-x, -y)$. In the code, the expansion centre (bubble centre) is located at $x = y = z = 0$, so we shift the cloud centre by Δr_0 in the xy plane:

$$x_0 = y_0 = \Delta r_0 / \sqrt{2}, \qquad z_0 = 0 \tag{18}$$

We assume a hydrogen abundance of $X = 0.735$, helium abundance of $Y = 0.245$, metallicity of $Z = 0.02$, and a mean relative particle weight of metals of 16.65. We also assume that all hydrogen in the cloud is in the form of H_2. This yields a mean relative particle weight of the molecular matter of $\mu = 2.34$. The molecular material of the cloud is isothermal with the temperature set at 20 K. We also consider the atomic gas component, which is represented by a density background with the constant value of 4 hydrogen atoms per $\rm cm^3$ and a temperature of 6000 K. The total initial energy of the bubble is set to 1×10^{49} erg and each time step δt the energy is increased by $\dot{E}\,\delta t$.

4.3. Comparison with Observation

We ran a series of simulations in order to find the parameters which produce a bubble with similar mass distribution and expansion velocity as N107. The varying input parameters for *ring* were the energy input ($\dot{E}$), the shift/dislocation of the expansion centre from the cloud centre (Δr_0), the gaussian thickness of the cloud in the direction of our line of sight (σ_z) and the total mass

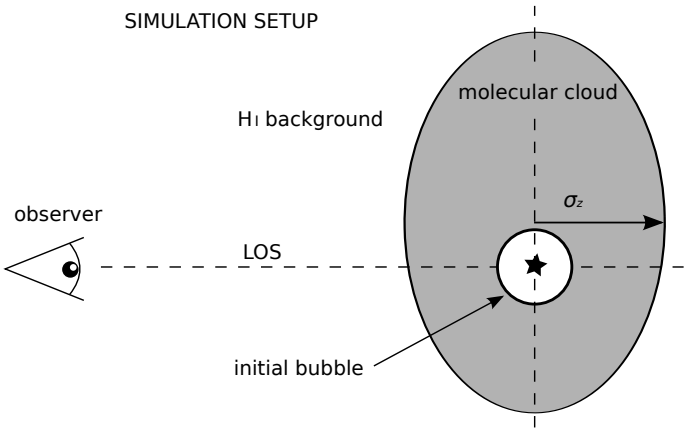

Fig. 9. Simulation setup for a stellar-blown bubble. The bubble is formed around a massive star(s) inside a molecular cloud, with a 3D gaussian density profile. The gaussian thickness σ_x and σ_y, in the sky plane, is set to 12 pc, while σ_z, which runs parallel to out LOS, is a parameter we vary. The centre of expansion is dislocated from the centre of the cloud by Δr_0, which is another parameter we vary. The dislocation is towards the $(-x, -y)$ direction, perpendicular to the LOS. The molecular cloud is overlaid over a background of atomic gas with the particle density of 4 cm^{-3}.

of the molecular cloud (M_0). The gaussian thickness in the sky plane $\sigma_{xy} = \sigma_x = \sigma_y$ was kept constant at 12 pc, which is comparable to the radius of N107. For each set of these parameters, the code evolves a bubble in time and outputs a chain of its snapshots in given time intervals.

Because the bubble is expanding in an inhomogeneous, nonspherical density field, the elements facing a lower density expand faster. This causes the bubble's geometrical centre to move progressively towards the direction of a lower density. To compensate for this drift, we centred each snapshot at the bubble's geometrical centre, which is computed as the mean (x, y, z) coordinates of the bubble elements weighted by their surfaces. We projected these centred snapshots onto FITS data cubes with two spatial (XY) and one radial velocity (RV) dimensions with the same pixel size as in the GRS data cube.

The radiation from OB stars illuminating molecular clouds creates a layer of dissociated matter. This layer then serves as a shield against the radiation and prevents it from penetrating further inside. The dissociated matter will not contribute to the ^{13}CO line brightness temperature. To account for that, before computing the ^{13}CO line brightness temperature, we decreased the surface density of each bubble element by 4.35 $M_\odot$ pc^{-2}. This value is based on the suggestion for shielding by Krumholz et al. (2009). We assume that the ^{13}CO abundances are the same as we used for measuring the observed molecular mass in sec. 2.4. Then we derived for each pixel the corresponding brightness temperature of the ^{13}CO (J = 1–0) line. Finally, we applied convolution to simulate the FCRAO telescope resolution used in the GRS. The resulting FITS thus represents an image, which would be seen by FCRAO if it observed the simulated bubble at a given evolution time.

We define a goodness-of-fit parameter δ, to compare the synthetic data cubes to the observations:

$$\delta = \frac{1}{3}\left[\delta V_{\rm exp}^2 + \frac{1}{4}\sum_{i=1}^{4}\left(\delta m_i^2 + \delta r_i^2\right)\right], \tag{19}$$

Table 3. Ranges of the input parameters $\dot{E}$, r_0, σ_z, M_0 and the constraint of the evolution time (t) we used for the numerical simulations of expanding bubbles.

Range of values	Steps
First series (wider parameter ranges)	
$\dot{E} = (0.1 \ldots 100) \times 10^{50}$ erg/Myr	10 log steps
$r_0 = (0.1 \ldots 30)$ pc	10 log steps
$\sigma_z = (1 \ldots 30)$ pc	10 log steps
$M_0 = (1 \times 10^5 \ldots 1 \times 10^7)\ M_\odot$	10 log steps
$t = (0 \ldots 100)$ Myr	0.5 Myr steps
Second series (finer)	
$\dot{E} = (0.1 \ldots 10) \times 10^{50}$ erg/Myr	8 log steps
$r_0 = (10 \ldots 28)$ pc	10 linear steps
$\sigma_z = (2 \ldots 28)$ pc	14 linear steps
$M_0 = (3 \times 10^5 \ldots 3 \times 10^6)\ M_\odot$	8 log steps
$t = (0 \ldots 8)$ Myr	0.25 Myr steps

Lower values of δ mean a better fit to (better agreement with) the observed properties of N107. The meaning of the terms is as follows:

$$\delta V_{\rm exp}^2 = \left(\frac{V_{\rm exp,\,s} - V_{\rm exp,\,o}}{V_{\rm exp,\,o}}\right)^2 \tag{20}$$

represents the square of the difference of the bubble expansion velocity between the observed value of N107 ($V_{\rm exp,\,o}$) and simulated value ($V_{\rm exp,\,s}$). We adopt the observed bubble expansion velocity of $V_{\rm exp,\,o}$ = 8 km/s, which is derived from the H I observations and represents half of the relative velocity of the shell's front and back wall.

$$\frac{1}{4}\sum_{i=1}^{4}\left(\delta m_i^2 + \delta r_i^2\right) = \frac{1}{4}\sum_{i=1}^{4}\left(\left[\frac{m_{i,\,\rm s} - m_{i,\,\rm o}}{m_{i,\,\rm o}}\right]^2 + \left[\frac{r_{i,\,\rm s} - r_{i,\,\rm o}}{r_{i,\,\rm o}}\right]^2\right) \tag{21}$$

is a sum taken over four circular sectors of the aperture 2 used for measuring the bubble molecular mass (see sec. 2.4). This term compares the angular mass distribution between N107 and the simulated bubbles. A visualisation of the sectors is show in fig. 10. $m_{i,\,\rm s}$ and $m_{i,\,\rm o}$ are the simulated ("s") and observed ("o") molecular masses in circular sector i. $r_{i,\,\rm s}$ and $r_{i,\,\rm o}$ give the simulated and observed mean radii in sector i, weighted by the brightness temperature:

$$r_i = \langle r_i \rangle_{T_{\rm b}} = \frac{\sum\limits_{(px\ \text{in}\ i)} r \cdot T_{\rm b}}{\sum\limits_{(px\ \text{in}\ i)} T_{\rm b}}, \tag{22}$$

where the sums are taken over the pixels in sector i.

First, we ran a series of simulations with a wider span of the input parameters $\dot{E}$, r_0, σ_z, M_0 with steps on a logarithmic scale and the evolution time up to t = 100 Myr with snapshots taken every 0.5 Myr. Then we located a subset of the input parameters with best fits to the observation (lowest δ) and ran a second series of simulations with finer parameter resolutions. In the second series, we used linear steps for parameters r_0 and σ_z and logarithmic steps for $\dot{E}$ and M_0. The snapshots were taken every 0.25 Myr up to t = 8 Myr. Note that the internal time step of *ring*

Table 4. First ten sets of parameters best fitting the observation of N107. $m_{1,2,3,4}$ are the masses of four sectors of the bubble. m_1/m_3 is the ratio of masses from the first and third sector, which quantify the mass contrast between the most and least massive sector. δ is a goodness-of-fit parameter (lower is better). The simulations are divided into two groups A and B, discussed at the end of sec. 4.3. Further explanation of the table columns is also given in sec. 4.3. The asterisk (*) marks two simulations – best of their group – which are visualised in fig. 10.

$\frac{\dot{E}}{10^{50}\ \mathrm{erg/Myr}}$	$\frac{r_0}{\mathrm{pc}}$	$\frac{\sigma_z}{\mathrm{pc}}$	$\frac{M_0}{10^5\ M_\odot}$	$\frac{t}{\mathrm{Myr}}$	$\frac{V_{\exp}}{\mathrm{km/s}}$	$\frac{m_1/m_2/m_3/m_4}{10^3\ M_\odot}$	$\frac{m_1}{m_3}$	$\frac{\delta}{10^{-2}}$	group
N107 observation									
					8.00	19.0 / 5.3 / 2.5 / 12.6	7.6		
Ten best fitting simulations									
0.2	18	6	5.8	2.25	7.85	14.8 / 6.8 / 2.2 / 6.8	6.7	3.42	A*
0.2	16	6	4.2	2.25	7.90	14.0 / 6.8 / 2.5 / 6.8	5.6	3.44	A
2.7	12	28	15.5	1.00	8.40	16.3 / 7.4 / 2.4 / 7.4	6.8	3.65	B*
2.7	12	20	11.2	1.00	8.55	16.2 / 7.4 / 2.4 / 7.4	6.8	3.73	B
2.7	12	26	15.5	1.00	8.25	16.7 / 7.8 / 2.6 / 7.8	6.4	3.82	B
2.7	10	26	11.2	1.00	8.20	14.5 / 7.2 / 2.8 / 7.2	5.2	3.85	B
2.7	10	28	11.2	1.00	8.35	14.1 / 6.8 / 2.5 / 6.8	5.6	3.88	B
0.4	22	6	15.5	1.75	8.50	17.1 / 7.6 / 2.1 / 7.6	8.1	3.89	A
0.2	20	6	8.0	2.25	8.05	15.8 / 6.5 / 1.7 / 6.5	9.3	3.96	A
2.7	10	20	8.0	1.00	8.50	14.0 / 6.8 / 2.6 / 6.8	5.4	3.96	B

is controlled dynamically by its Runge-Kutta routines; we only set the snapshot printout interval Δt. Parameters for both runs are listed in table 3. The ten best fitting runs are shown in table 4.

To conclude, we simulated the evolution of bubbles formed around massive stars in molecular clouds and compared their properties to N107. We got the best agreement for two groups of parameters:

1. Group A represents bubbles produced with a lower energy input ($\dot{E} < 0.4 \times 10^{50}$ erg/Myr), greater centre-of-expansion dislocation ($r_0 \approx 16 \ldots 22$ pc), formed within an oblate molecular cloud with the oblateness of ($\sigma_z/\sigma_{xy} = 6/12$), and with a greater evolution time ($t \approx 1.75 \ldots 2.25$ Myr).
2. Group B represents bubbles produced with a higher energy input ($\dot{E} = 2.7 \times 10^{50}$ erg/Myr), smaller centre-of-expansion dislocation ($r_0 \approx 10 \ldots 12$ pc), formed within a prolate molecular cloud ($\sigma_z/\sigma_{xy} \approx (20 \ldots 28)/12$), with a smaller evolution time ($t = 1$ Myr).

Fits show little sensitivity to the parameter M_0 – the initial mass of the surrounding molecular cloud ($M_0 \approx 5.8 \ldots 15.5 \times 10^5\ M_\odot$). Both groups of the best-fittings-simulations suggest that bubble N107 is relatively young ($t \lessapprox 2.25$ Myr) and was formed at the very edge of its parental molecular cloud.

Fig. 10 shows snapshots from the best fitting simulations from both groups A and B and the GRS observation of the CO line.

5. Discussion

5.1. Numerical Simulation Setup, Assumptions and Validity of Approximations

An important assumption for the simulation setup is the shape and density profile of the parental molecular cloud. In our simulations, we chose the gaussian density profile and tested different levels of the oblateness (ratio of σ_z to σ_{xy}). The oblate shape of the parental molecular clouds which host bubbles similar to N107 is supported by a study of Beaumont & Williams (2010), who concluded that the Spitzer bubbles are formed in oblate, sheet-like, molecular clouds with a thickness of a few parsecs. Our simulations, however, favour neither oblate nor prolate clouds.

The numerical code *ring* assumes the thin-shell approximation, which is applicable so long as the bubble expansion is supersonic, i.e. expanding with a velocity higher than the sound speed of the ambient cold gas: ≈ 0.3 km/s (for $T = 20$ K, $\gamma = 7/5$, $\mu = 2.34$). In our runs, almost all the bubble's elements move faster through the ambient gas during the whole bubble evolution, so the thin-shell approximation is reasonable. Moreover, if the speed of an element decreases below the sound speed, the code stops the mass accumulation for that element.

5.2. Source of Radio Continuum

The radio continuum emission coming from the direction of the bubble interior has both thermal and nonthermal components. While the strong radio source A is dominated by nonthermal radiation, fainter source B is emitting thermally (fig. 6). The nonthermal source A is brighter than the thermal source B by almost one order of magnitude, so we can expect that the thermal emission is present in the whole bubble volume, only outshone in aperture A by the nonthermal source. Mixing of thermal and nonthermal radiation in aperture A is also suggested by the visual comparison of the radio continuum and the 24 μm emission (fig. 7). The northern part of aperture A features both the radio continuum and the 24 μm emission, while in the southern part only the radio continuum is observed. Further, merging of thermal and nonthermal radiation in aperture A explains why the measured spectral index (−0.3) is closer to 0 than the typical value for supernova remnants (−0.5, the average value in the SNRs catalogue of Green 2009).

The negative spectral indices of sources C (−0.2) and D (−0.1) suggest that part of their radio continuum is also emitted by a nonthermal source. The nonthermal contribution to the flux is stronger for source C than for source D. This is expected, since aperture D covers a distinct 24 μm (thermal) source, while there is almost no 24 μm emission in aperture C (fig. 7).

Given that first supernovae in an OB association explode only after 3 Myr or later, and considering the bubble evolution time estimated from simulations (< 2.25 Myr), no supernova remnant should be present inside the bubble, yet. In other words,

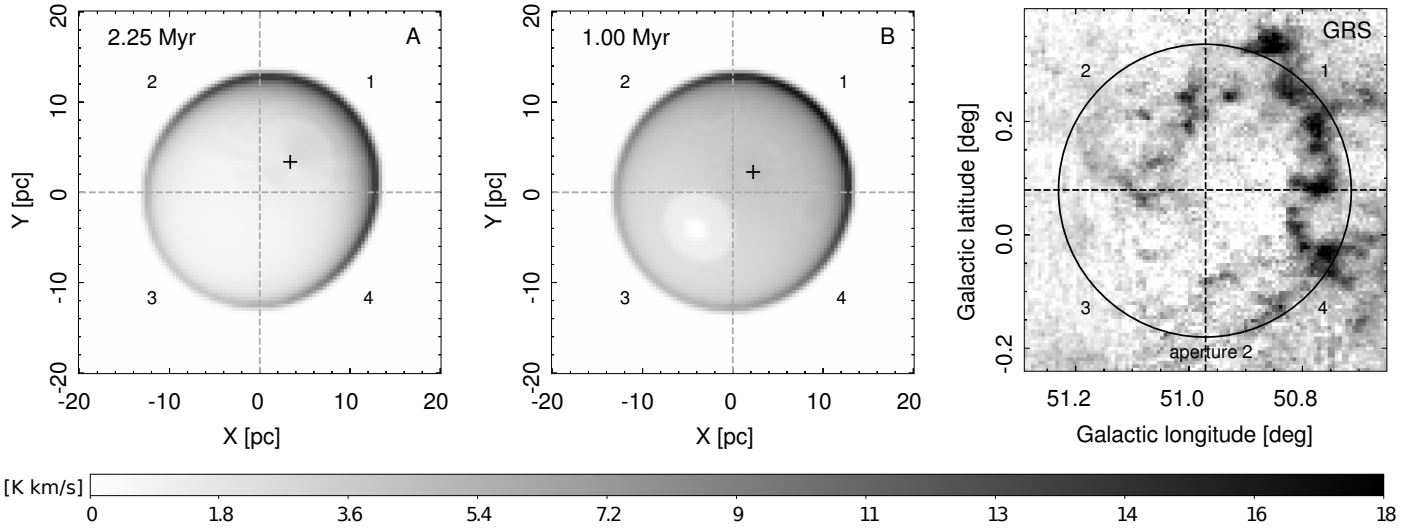

Fig. 10. Snapshots from the best fitting simulations from group A (left) and B (centre) and GRS observation (right). Shown is the brightness temperature of the ^{13}CO line integrated over the radial velocities of ±8 km/s relative to the radial velocity of the bubble centre. The images also show four sectors used for comparing the angular mass distribution (see sec. 4.3 and eq. 21). The plus sign (+) in pictures A and B marks the original expansion centre. Aperture 2, shown in the GRS picture, marks which region from the observed data we used for comparison with simulations.

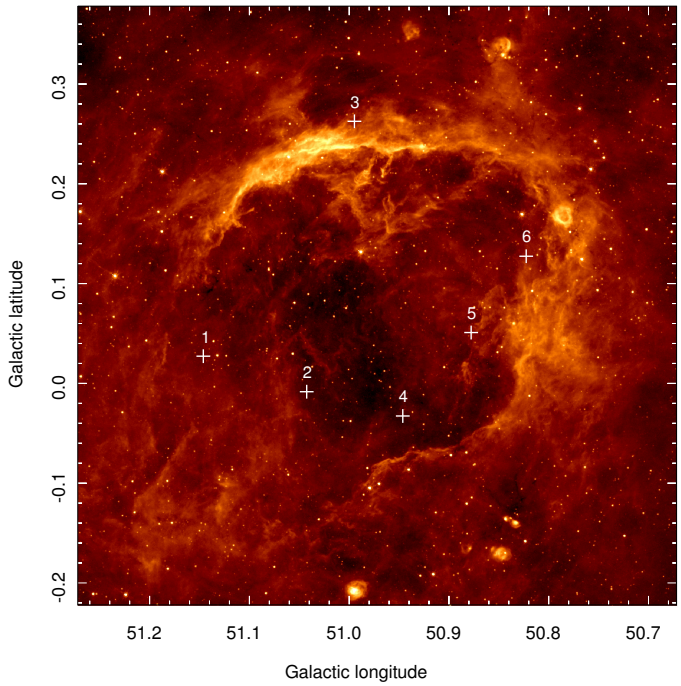

Fig. 11. Possible stellar progenitors (white plus signs) of bubble N107 found in the UKIDSS catalogue. The numerical labels of the stars correspond to the labels in table 5. The background is the 8 μm emission taken from GLIMPSE.

our analysis suggests that a supernova remnant, not associated with the bubble, may be present in the direction towards the bubble.

5.3. Missing OB Association

We searched the SIMBAD database and a catalogue of Galactic OB stars by Reed (2003) for sources which could be responsible for the bubble creation. However, no OB star, supernova remnant or pulsar is known to lie in the direction of the bubble interior or in its vicinity.

We also performed a search for massive stars possibly related to N107 using the UKIDSS catalogue 7th data release (Lawrence et al. 2007), stellar evolutionary tracks by Bressan et al. (2012) and the standard model of extinction (Rieke & Lebofsky 1985). We derived the extinction for the massive star candidates in the field of N107 and compared it to the values of extinction given for that direction by Stead & Hoare (2009). The search for massive stars involves many uncertainties, but the comparison of the derived extinctions with independent values is a good test of the credibility of our results. We ended up with six massive star candidates, which lie at distances comparable with the distance of N107 (3.6 kpc). None of these six stars have measured radial velocities. Three of them lie at the rim of the bubble, so they can hardly be its progenitors, but the others are possible energy sources. The selected massive stars are shown in fig. 11 and listed in table 5.

5.4. Molecular Clump Mass Spectrum

The best fitting slope for the mass spectrum of molecular clumps found along the borders of N107 is −1.1 (fig. 8). This is a significantly shallower slope than that of the classical stellar initial mass function (Salpeter: −2.35) and also shallower than the clump mass function slope of −1.6 to −1.8 derived by Kramer et al. (1998). Note that Kramer et al. (1998) used gaussian decomposition for clump identification, which is a fundamentally different method than we used and, moreover, studied different types of clouds – not shell-like as is our case of N107.

The least massive clumps we found have masses about 3.5 $M_\odot$. This limit is given by the angular resolution and sensitivity of the observations of the ^{13}CO line. With better resolution and sensitivity, we expect that some clumps, especially the most massive ones, would be identified as several less massive clumps. This would alter the shape of the clump mass spectrum, and likely redistribute the mass of the largest clumps into less massive ones, so that the slope would be steeper.

Table 5. Possible stellar progenitors of bubble N107 found in the UKIDSS catalogue. First column gives the source label as marked in fig. 11. Second column gives the ID from the UKIDSS catalogue. Third and fourth columns give the galactic longitude and latitude. Fifth column gives the estimated mass of the source and sixth column gives the estimated distance.

label in fig. 11	source ID (UKIDSS)	$\frac{l}{\deg}$	$\frac{b}{\deg}$	$\frac{\text{mass}}{M_\odot}$	$\frac{\text{distance}}{\text{kpc}}$
1	438326491324	51.1461745	+0.0272455	8.00	3.705
2	438326507390	51.0425744	−0.0083589	9.00	4.044
3	438326996219	50.9947238	+0.2626358	9.00	4.112
4	438328069418	50.9462654	−0.0326783	9.00	3.193
5	438328066620	50.8777609	+0.0509439	9.00	3.219
6	438328834208	50.8225691	+0.1274098	9.00	3.232

6. Conclusion

We studied dust bubble N107, discovered by Churchwell et al. (2006) with infrared observations by the Spitzer Space Telescope. Radio observations of the H I and ^{13}CO ($J = 1-0$) lines revealed its atomic and molecular components, which allowed us to determine the bubble radial velocity, kinematical distance and mass of these components. Using the code DENDROFIND (Wünsch et al. 2012) we decomposed the molecular ring associated with the bubble into 49 individual clumps and found that the clump mass spectrum slope is about −1.1. Radio continuum observations at 1420 and 327 MHz suggest the radio flux coming from the bubble direction has both thermal and nonthermal components; i.e., besides a classical H II region, a supernova remnant contributes to the emission. We simulated the evolution of stellar-blown bubbles within molecular clouds with the numerical code *ring* (Palouš 1990; Ehlerová & Palouš 1996). We were able to produce two groups of bubbles with a similar angular mass distribution and expansion velocity as N107: **(A)** Bubbles formed within an oblate molecular cloud ($\sigma_z/\sigma_{xy} = 6/12$), with the energy input $\dot{E} < 0.4 \times 10^{50}$ erg/Myr and the evolution time $t \approx 1.75 \ldots 2.25$ Myr. **(B)** Bubbles formed within a prolate molecular cloud ($\sigma_z/\sigma_{xy} = (20 \ldots 28)/12$), with the energy input $\dot{E} \approx 2.7 \times 10^{50}$ erg/Myr and the evolution time $t = 1$ Myr. Considering the estimated bubble evolution time (< 2.25 Myr), no supernova remnant should be present inside the bubble, yet. This may be explained by a supernova remnant present in the direction towards the bubble, however not associated with it. A summary of the parameters we derived for bubble N107, together with the parameters given by Churchwell et al. (2006), is presented in table 6.

Acknowledgements. We thank to the anonymous referee for multiple constructive suggestions which led to improvements of the paper. This work was supported by the project RVO: 67985815. VS acknowledges support from a Marie Curie fellowship as part of the European Commission FP6 Research Training Network 'Constellation' under contract MCRTN–CT–2006-035890; support from Doctoral grant of the Czech Science Foundation No. 205/09/H033. RW acknowledges support from the project P209/12/1795 of the Czech Science Foundation. The research leading to these results has received funding from the European Community's Seventh Framework Programme under grant agreement no. PIIF-GA-2008-221289. This research has made use of SAOImage DS9, developed by Smithsonian Astrophysical Observatory (Joye & Mandel 2003). This research has made use of the SIMBAD database, operated at CDS, Strasbourg, France. This research has made use of NASA's Astrophysics Data System. This research has made use of the NASA/IPAC Infrared Science Archive, which is operated by the Jet Propulsion Laboratory, California Institute of Technology, under contract with the National Aeronautics and Space Administration. This publication has made use of molecular line data from the Boston University-FCRAO Galactic Ring Survey (GRS). The GRS is a joint project of Boston University and Five College Radio Astronomy Observatory, funded by the National Science Foundation under grants AST-9800334, AST-0098562, & AST-0100793.

Table 6. Summary of parameters derived for N107. The first section gives the values from the original catalogue of Churchwell et al. (2006). The second section gives the values derived from observation (sec. 2). The third section gives the values estimated from simulations (sec. 4).

Property	Value
From catalogue of Churchwell et al. (2006)	
Galactic longitude (central)	50.°972
Galactic latitude (central)	0.°078
Angular radius (mean)	11.′39
Angular thickness (mean)	2.′26
Derived from observations	
Radial velocity (central)	43 km/s
Expansion velocity	8 km/s
Distance (kinematical)	3.6 kpc
Radius (mean)	11.9 pc
Mass in H I (aperture 1)	$(5.4 \pm 1.0) \times 10^3\ M_\odot$
Mass of molecular component (aperture 1)	$(1.3 \pm 0.4) \times 10^5\ M_\odot$
Mass of molecular component (aperture 2)[1]	$(4.0 \pm 1.2) \times 10^4\ M_\odot$
Estimated from simulations	
Energy input rate	$< 0.4 \times 10^{50}$ erg/Myr^A
	$\approx 2.7 \times 10^{50}$ erg/Myr^B
Dislocation of expansion centre	$\approx 16 \ldots 22$ pc^A
	$\approx 10 \ldots 12$ pc^B
Parental cloud thickness in LOS	≈ 6 pc^A
	$\approx 20 \ldots 28$ pc^B
Parental cloud total mass	$\approx 5.8 \ldots 15.5 \times 10^5\ M_\odot$
Evolution time (age)	$\approx 1.75 \ldots 2.25$ Myr^A
	≈ 1Myr^B

Notes. [1] Aperture 2 covers only the immediate vicinity of the bubble. See fig. 4 for an illustration. [A] Estimated from simulations from group A. [B] Estimated from simulations from group B.

References

Beaumont, C. N. & Williams, J. P. 2010, ApJ, 709, 791
Benjamin, R. A., Churchwell, E., Babler, B. L., et al. 2003, PASP, 115, 953
Binney, J. & Merrifield, M. 1998, Galactic Astronomy, ed. Binney, J. & Merrifield, M.
Brand, J. & Blitz, L. 1993, A&A, 275, 67
Bressan, A., Marigo, P., Girardi, L., et al. 2012, MNRAS, 427, 127
Carey, S. J., Noriega-Crespo, A., Mizuno, D. R., et al. 2009, PASP, 121, 76
Casali, M., Adamson, A., Alves de Oliveira, C., et al. 2007, A&A, 467, 777
Castor, J., McCray, R., & Weaver, R. 1975, ApJ, 200, L107
Chevalier, R. A. 1974, ApJ, 188, 501
Churchwell, E., Povich, M. S., Allen, D., et al. 2006, ApJ, 649, 759

Condon, J. J. & Ransom, S. M. 2010, Essential Radio Astronomy (National Radio Astronomy Observatory), [online; http://www.cv.nrao.edu/course/astr534/ERA.shtml]
Deharveng, L., Schuller, F., Anderson, L. D., et al. 2010, A&A, 523, A6
Dib, S. & Burkert, A. 2005, ApJ, 630, 238
Draine, B. T. 2003, ARA&A, 41, 241
Duvert, G., Cernicharo, J., Bachiller, R., & Gomez-Gonzalez, J. 1990, A&A, 233, 190
Efremov, Y. N., Ehlerová, S., & Palouš , J. 1999, A&A, 350, 457
Efremov, Y. N., Elmegreen, B. G., & Hodge, P. W. 1998, ApJ, 501, L163+
Ehlerová, S. & Palouš, J. 1996, A&A, 313, 478
Ehlerová, S. & Palouš, J. 2005, A&A, 437, 101
Elmegreen, B. G. 1994, ApJ, 427, 384
Elmegreen, B. G. & Lada, C. J. 1977, ApJ, 214, 725
Green, D. A. 2009, VizieR Online Data Catalog, 7253, 0
Hambly, N. C., Collins, R. S., Cross, N. J. G., et al. 2008, MNRAS, 384, 637
Heiles, C. 1979, ApJ, 229, 533
Heiles, C. 1984, ApJS, 55, 585
Hewett, P. C., Warren, S. J., Leggett, S. K., & Hodgkin, S. T. 2006, MNRAS, 367, 454
Irwin, M. J., Lewis, J., Hodgkin, S., et al. 2004, in Society of Photo-Optical Instrumentation Engineers (SPIE) Conference Series, Vol. 5493, Optimizing Scientific Return for Astronomy through Information Technologies, ed. P. J. Quinn & A. Bridger, 411–422
Jackson, J. M., Rathborne, J. M., Shah, R. Y., et al. 2006, ApJS, 163, 145
Joye, W. A. & Mandel, E. 2003, in Astronomical Society of the Pacific Conference Series, Vol. 295, Astronomical Data Analysis Software and Systems XII, ed. H. E. Payne, R. I. Jedrzejewski, & R. N. Hook, 489
Kahn, F. D. 1954, Bull. Astron. Inst. Netherlands, 12, 187
Kellermann, K. I. & Verschuur, G. L. 1988, Galactic and extragalactic radio astronomy (2nd edition)
Kiss, C., Moór, A., & Tóth, L. V. 2004, A&A, 418, 131
Könyves, V., Kiss, C., Moór, A., Kiss, Z. T., & Tóth, L. V. 2007, A&A, 463, 1227
Koo, B.-C., Gibson, S. J., Kang, J.-h., et al. 2010, Highlights of Astronomy, 15, 788
Kramer, C., Stutzki, J., Rohrig, R., & Corneliussen, U. 1998, A&A, 329, 249
Krumholz, M. R., McKee, C. F., & Tumlinson, J. 2009, ApJ, 693, 216
Lawrence, A., Warren, S. J., Almaini, O., et al. 2007, MNRAS, 379, 1599
Lefloch, B. & Lazareff, B. 1994, A&A, 289, 559
Loeb, A. & Perna, R. 1998, ApJ, 503, L35+
MacLaren, I., Richardson, K. M., & Wolfendale, A. W. 1988, ApJ, 333, 821
Oort, J. H. & Spitzer, Jr., L. 1955, ApJ, 121, 6
Paladini, R., Burigana, C., Davies, R. D., et al. 2003, A&A, 397, 213
Palouš, J. 1990, in IAU Symposium, Vol. 144, IAU Symposium, 101P
Pavlyuchenkov, Y. N., Kirsanova, M. S., & Wiebe, D. S. 2013, Astronomy Reports, 57, 573
Peek, J. E. G., Heiles, C., Douglas, K. A., et al. 2011, ApJS, 194, 20
Reach, W. T., Rho, J., Tappe, A., et al. 2006, AJ, 131, 1479
Reed, B. C. 2003, AJ, 125, 2531
Rieke, G. H. & Lebofsky, M. J. 1985, ApJ, 288, 618
Rohlfs, K. & Wilson, T. L. 1996, Tools of Radio Astronomy, ed. Rohlfs, K. & Wilson, T. L.
Rosolowsky, E. W., Pineda, J. E., Kauffmann, J., & Goodman, A. A. 2008, ApJ, 679, 1338
Simpson, R. J., Povich, M. S., Kendrew, S., et al. 2012, MNRAS, 424, 2442
Sonnentrucker, P., Welty, D. E., Thorburn, J. A., & York, D. G. 2007, ApJS, 168, 58
Spitzer, L. 1978, Physical processes in the interstellar medium
Stead, J. J. & Hoare, M. G. 2009, MNRAS, 400, 731
Stil, J. M., Taylor, A. R., Dickey, J. M., et al. 2006, AJ, 132, 1158
Taylor, A. R., Goss, W. M., Coleman, P. H., van Leeuwen, J., & Wallace, B. J. 1996, ApJS, 107, 239
Tenorio-Tagle, G. & Bodenheimer, P. 1988, ARA&A, 26, 145
Visser, R., van Dishoeck, E. F., & Black, J. H. 2009, A&A, 503, 323
Weaver, R., McCray, R., Castor, J., Shapiro, P., & Moore, R. 1977, ApJ, 218, 377
Whitworth, A. P., Bhattal, A. S., Chapman, S. J., Disney, M. J., & Turner, J. A. 1994, MNRAS, 268, 291
Wilson, T. L. 1999, Reports on Progress in Physics, 62, 143
Wünsch, R., Jáchym, P., Sidorin, V., et al. 2012, A&A, 539, A116

Appendix A: List of Molecular Clumps

Table A.1. Molecular clumps associated with bubble N107. First column gives a number identifying a clump in our list. The meaning of other columns is explained in sec. 3. This is the full list expanding tab. 2.

N	$\frac{l_{\rm peak}}{\rm deg}$	$\frac{b_{\rm peak}}{\rm deg}$	$\frac{v_{\rm peak}}{\rm km\ s^{-1}}$	$\frac{T_{\rm peak}}{\rm K}$	$\frac{R}{\rm pc}$	$\frac{\rm FWHM_l}{\rm pc}$	$\frac{\rm FWHM_b}{\rm pc}$	$\frac{\rm FWHM_v}{\rm km\ s^{-1}}$	$\frac{M}{M_\odot}$	$\frac{\Delta M}{M_\odot}$	$\frac{M_{\rm vir}}{M_\odot}$	$\frac{\Delta M_{\rm vir}}{M_\odot}$	$\frac{M}{M_{\rm vir}}$
1	50.919	0.241	41.89	7.0	2.2	2.45	1.62	1.84	1037.1	5.6	1409.9	324.8	0.736
2	50.840	0.266	44.01	5.8	4.0	3.48	3.40	2.83	4082.1	11.5	6050.2	909.0	0.675
3	50.753	-0.029	45.08	4.7	3.2	3.38	2.52	4.63	3119.8	10.8	12847.9	1180.5	0.243
4	51.073	0.204	45.93	4.7	1.2	1.41	0.99	2.57	351.1	3.6	1494.4	247.5	0.235
5	50.766	0.081	45.50	4.6	3.3	3.66	2.21	3.92	3469.1	10.9	9622.4	1044.0	0.361
6	50.938	-0.072	42.31	4.6	1.8	3.06	1.17	1.70	635.2	4.8	1010.1	252.4	0.629
7	50.778	0.192	42.74	4.5	5.0	5.15	5.07	2.76	7365.5	15.9	7259.4	1120.0	1.015
8	50.815	0.020	42.10	4.5	2.3	1.59	2.60	3.91	1206.7	6.8	6597.7	716.4	0.183
9	50.803	-0.029	44.01	4.4	2.3	2.05	2.11	2.26	1059.1	6.1	2272.7	428.0	0.466
10	50.999	0.247	43.59	3.6	1.4	2.08	1.08	2.26	276.5	3.5	1343.3	252.2	0.206
11	50.858	-0.048	42.95	3.3	1.2	1.72	0.86	1.55	169.3	2.8	560.8	154.1	0.302
12	50.796	0.124	44.01	2.5	1.4	1.27	1.41	1.44	149.6	2.7	554.4	164.0	0.270
13	50.784	0.131	46.56	2.3	0.9	0.87	1.09	0.96	45.3	1.5	152.0	67.4	0.298
14	50.870	-0.152	40.83	2.1	1.0	1.22	1.06	1.42	60.9	1.7	366.1	109.3	0.166
15	50.969	-0.128	39.34	2.0	0.8	1.01	0.87	0.58	26.3	1.2	53.4	39.3	0.493
16	50.883	0.297	43.80	1.9	0.5	0.88	0.46	0.47	8.4	0.7	20.0	18.3	0.417
17	50.913	0.180	46.35	1.9	0.9	1.61	0.93	1.09	48.5	1.6	197.8	77.0	0.245
18	50.913	0.155	41.68	1.8	0.6	0.84	0.67	0.46	11.7	0.8	25.2	23.1	0.465
19	50.864	0.210	45.29	1.8	0.5	0.68	0.52	1.11	15.6	0.9	114.0	43.7	0.137
20	50.833	0.210	40.19	1.7	1.0	1.36	1.06	0.81	26.3	1.2	120.1	63.4	0.219
21	50.833	0.057	42.95	1.7	0.5	0.73	0.76	0.21	5.0	0.5	4.6	9.2	1.088
22	50.864	0.260	41.04	1.7	0.4	0.73	0.50	0.41	5.8	0.5	14.2	14.6	0.411
23	50.987	-0.171	41.46	1.6	0.5	0.96	0.58	0.21	4.0	0.5	4.2	8.4	0.950
24	50.956	-0.122	40.40	1.6	0.8	1.27	1.06	0.79	22.7	1.1	99.3	53.6	0.228
25	50.790	0.014	38.91	1.6	0.6	0.85	0.79	0.30	6.2	0.6	9.7	13.8	0.639
26	50.870	-0.042	39.55	1.6	0.8	1.02	1.00	0.59	17.8	1.0	54.8	39.2	0.326
27	50.735	0.051	39.76	1.6	0.6	1.02	0.59	0.41	8.7	0.7	19.3	20.2	0.449
28	50.846	0.192	39.13	1.5	0.4	0.79	0.57	0.31	4.4	0.5	8.0	11.0	0.548
29	50.833	-0.066	41.68	1.5	0.5	0.95	0.57	0.27	4.6	0.5	7.0	10.8	0.661
30	50.889	-0.036	39.76	1.5	0.4	0.59	0.55	0.32	3.8	0.5	7.4	9.8	0.519
31	51.061	-0.042	45.71	1.5	0.5	0.89	0.49	0.48	5.5	0.5	21.5	19.0	0.255
32	50.981	0.026	43.80	1.5	0.5	0.98	0.59	0.21	4.0	0.5	4.2	8.4	0.955
33	50.778	0.032	46.78	1.5	0.6	0.96	0.56	0.48	9.6	0.7	24.9	22.2	0.383
34	50.864	0.087	42.31	1.4	0.5	0.77	0.76	0.21	4.2	0.5	4.2	8.4	0.992
35	50.981	-0.152	46.14	1.4	0.5	0.80	0.59	0.21	3.8	0.5	4.2	8.4	0.899
36	50.987	0.038	46.99	1.4	0.4	0.53	0.81	0.33	3.8	0.5	8.8	11.5	0.426
37	50.864	0.192	42.10	1.4	0.5	0.70	0.71	0.61	8.0	0.7	38.3	26.5	0.210
38	51.006	0.247	45.50	1.4	0.3	0.59	0.39	0.42	3.8	0.5	10.3	10.5	0.370
39	50.969	0.327	46.78	1.3	0.6	1.02	0.59	0.30	5.6	0.6	10.2	14.2	0.554
40	50.956	-0.109	46.35	1.3	0.5	0.52	1.10	0.21	3.5	0.5	4.2	8.4	0.844
41	50.956	-0.091	46.99	1.3	0.5	1.06	0.57	0.21	4.4	0.5	4.6	9.2	0.964
42	50.969	0.327	41.89	1.3	0.4	0.73	0.50	0.32	4.6	0.5	8.5	11.3	0.538
43	50.852	-0.017	45.29	1.3	0.4	0.83	0.53	0.29	3.6	0.5	6.9	10.2	0.521
44	50.741	0.051	42.10	1.3	0.5	0.69	0.78	0.21	3.7	0.5	4.2	8.4	0.892
45	50.821	0.241	39.55	1.3	0.6	0.59	1.11	0.33	7.8	0.7	11.8	15.3	0.665
46	50.815	-0.066	42.95	1.2	0.5	1.15	0.56	0.40	5.7	0.6	16.0	17.1	0.356
47	51.221	0.081	46.78	1.2	0.5	0.71	0.71	0.32	5.6	0.6	10.6	13.9	0.526
48	51.067	0.149	45.93	1.2	0.4	0.53	0.78	0.29	3.5	0.5	6.9	10.1	0.513
49	50.796	0.223	41.04	1.2	0.4	1.01	0.39	0.29	3.4	0.5	7.0	10.2	0.485